Rare Met. (2018) 37(5):413–420
https://doi.org/10.1007/s12598-018-1030-1

RARE METALS
www.editorialmanager.com/rmet

Crystallization mechanism of glass-ceramics prepared from stainless steel slag

Wen-Di Fan, Qiang-Wei Yang, Bin Guo, Bo Liu, Shen-Gen Zhang*

Received: 6 December 2017 / Revised: 1 March 2018 / Accepted: 14 March 2018 / Published online: 20 April 2018

Abstract Glass-ceramics have been prepared by using stainless steel slag, fly ash and coal fly ash that were fig- obtained from industrial solid waste. The crystallization behavior and mechanical characterization of the glass-ceramics with different $(CaO + MgO)/(SiO_2 + Al_2O_3)$ content ratios were studied. While the basicity decreases from 1.2 to 0.9 cm^{-3}, the bridge oxygen content increases from 1.18×10^{21} to 1.34×10^{21} cm^{-3}. According to the deconvolution of Raman spectra, the relative abundance of the stretching of $Si–O_{nb}$ bond (Q^n units) can be obtained. The increase in the Q^3 units dominates the polymerization in the process of decreasing basicity. This change in bonding is demonstrated to lead to polymerization of the glass network and the increase in crystallization activation energy from 336.0 to 360.7 $kJ·mol^{-1}$. The results demonstrate that the production of the glass-ceramics from industrial steel slag, fly ash and coal fly ash is cost-effective and offers advantages over other production methods.

Keywords Glass-ceramics; Stainless steel slag; Augite

1 Introduction

Glass-ceramics have a number of valuable properties, including high mechanical strength, thermal shock and wear and chemical resistance [1–4]. Glass-ceramics can be used for many different applications, e.g., high-temperature insulators, biomedical materials, abrasion-resistant linings and insulation materials. Glass-ceramics that are made from solid wastes are beneficial to lower production costs and are environmentally sustainable.

Recently, different types of solid wastes, such as municipal waste incineration plant fly ash, steel industry dust, zinc hydrometallurgy wastes, cooper flotation waste and municipal waste incineration have been investigated as production sources for glass-ceramics materials [5–7]. The composition of solid waste is complex as it contains many different kinds of oxides. Complex mixtures of various oxides in glass-ceramics are affecting the resulting properties. Although the raw materials contain many kinds of oxides, SiO_2, Al_2O_3, CaO and MgO have the greatest influence on the material properties of glass-ceramics and are the most common components in solid waste. The impact of oxides on a glass network can be divided into three groups: glass-forming oxides, modifier oxides and amphoteric oxides. The acidic oxide, SiO_2, is a glass-forming oxide from a glass framework [8]. Alkaline oxides, such as CaO and MgO, are modifier oxides that replace silicon cations in the glass structural frame works [9]. Al_2O_3 is an example of amphoteric oxide that can form a tetrahedral glass framework.

Recently, the ratio of modifier oxides in glass-forming oxides has been widely studied. Partyka et al. [9] reported the effect of ratio of SiO_2 to Al_2O_3 on the structure and microstructure of the glasses in the $CaO–MgO–Al_2O_3–SiO_2$ (CMAS) system. These previously reported results showed that the presence of Al_2O_3 in the glass network created a more compact material. Xiao et al. [10] investigated the microstructure and properties of CMAS glass-ceramics with different CaO/MgO ratios. The results reported showed that lower content ratios of CaO/MgO increased the crystallization temperature of the glass. There were also reported on the crystallization and mechanical

W.-D. Fan, Q.-W. Yang, B. Guo, B. Liu, S.-G. Zhang*
Institute for Advanced Materials and Technology, University of Science and Technology Beijing, Beijing 100083, China
e-mail: zhangshengen@mater.ustb.edu.cn

properties of glass-ceramics with the cation content of network modified by the addition of Ca^{2+}, Mg^{2+} and Na^{+} [1, 11–14]. These studies show that the modifier oxides could promote the glass crystallization of CAMS glass-ceramics. However, there are few reports on glass-ceramics prepared with different ratios of modifier oxides in glass-forming oxides.

In this work, the basicity was used to represent the content of CaO and MgO modifier oxides which were added to SiO_2 and Al_2O_3 glass-forming oxides. Al_2O_3 is mostly incorporated into the glass network as $[AlO_4]$ tetrahedra due to a charge balanced by excess network former. Also, the CaO–MgO–Al_2O_3–SiO_2 glass-ceramics with different ratios of basicity were studied. The basicity of the batches was reported to a range between 0.9 and 1.2 when adjusting the steel slag and fly ash contents. The purpose of this study was to investigate the effects of basicity on glass-ceramics and obtain glass-ceramics with functional properties and a wider processing window.

2 Experimental

2.1 Chemical compositions of samples

Steel slag was obtained from a steel plant in Taiyuan, China. Fly ash was collected from a municipal solid waste incineration (MSWI) plant in Wuhan, China. The coal fly ash was obtained from the Shenhua Power Station, Taicang, China. The coal fly ash is of coal origin. Chemical composition was investigated by X-ray fluorescence (XRF, XRF-1800), and the main chemical compositions of raw materials are summarized in Table 1. Coal fly ash is the main source of SiO_2 and Al_2O_3. The basicity of glass-ceramics is achieved by adding different contents of coal fly ash. The ratio of the batch of GC-1, GC-2 and GC-3 samples containing fly ash, steel slag and coal fly ash is 1.00:1.00:0.86, 1.00:1.00:1.14 and 1.00:1.00:1.42, respectively, as listed in Table 2. Homogeneous mixtures of the batches were obtained by dry mixing for 1 h in a ball mill.

2.2 Glass preparation

The mixture of raw materials was packed in a corundum crucible and melted at 1450 °C for 2 h. The melts were then poured into an iron mold (preheated at 600 °C) and were soaked for 30 min to produce the parent glasses.

2.3 Thermal analysis

Thermal analysis of the parent glass powder samples was conducted by a differential scanning calorimeter (DSC, SDT Q600). The heating rates used were 10, 15 and 25 °C·min^{-1} from room temperature to 1000 °C. In order to minimize the effect of surface crystallization, bulk samples (small plates of glass broken off a thin glass sheet) were used. The sensitivity of SDT Q600 is 0.001 °C.

2.4 Properties analysis of glass-ceramics

The Vickers microhardness of the specimens was measured by the Vickers hardness test instrument (MH-6, China), using the average of 5 tests.

The density (ρ) of glass-ceramics was determined at 25 °C through the Archimedes principle by using water as the medium and using the average of 5 tests. The error in this method was determined based on repetitive measurements. Firstly, the sample was weighed in air (m_1) and then measured in an immersion distilled water (m_2) with density of ρ_{dw} = 1 g·cm^{-3}. The density of the samples was then calculated using the following equation:

$$\rho = m_1\rho_{dw}/(m_1 - m_2). \quad (1)$$

The CDW-5(China) was employed to test the bending strength using the 3-point bending geometry. Samples were cut from a block of glass-ceramics with dimensions of 40 mm × 4 mm × 3 mm. For each sample, polishing was done with SiC paper to avoid any difference in roughness on the surfaces. The bending strength measurement was considering the crosshead speed of 0.5 mm·min^{-1} with a span length of 30 mm. Five measurements were made, and the mean values were calculated.

Water absorption of glass-ceramics was measured after 3-h immersion in boiling distilled water, determined by the

Table 1 Chemical compositions of raw materials (wt%)

Materials	CaO	MgO	SiO_2	Al_2O_3	Fe_2O_3	Cr_2O_3	Cl	TiO_2	P_2O_5	Na_2O	K_2O	Others
Fly ash	42.29	2.58	8.12	2.41	3.47	0.06	17.24	1.22	–	7.55	5.86	8.21
Steel slag	49.73	12.51	27.81	3.42	0.43	4.53	–	0.02	–	–	–	1.55
Coal fly ash	10.14	1.14	53.99	18.41	9.47	0.037	–	1.35	0.27	1.03	2.74	1.42

Others: ZnO, BaO, CuO, MnO, BaO, Co_2O_3

Table 2 Chemical compositions of batch (g) and ratio of (CaO + MgO)/(SiO_2 + Al_2O_3)

Samples	CaO	MgO	SiO_2	Al_2O_3	Fe_2O_3	Cr_2O_3	TiO_2	P_2O_5	Na_2O	K_2O	(CaO + MgO)/(SiO_2 + Al_2O_3)
GC-1	35.24	3.53	28.77	7.55	4.05	1.62	0.70	0.51	2.95	2.87	1.2
GC-2	32.96	3.32	31.06	8.54	4.55	1.47	0.76	0.49	2.78	2.86	1.0
GC-3	31.06	3.14	32.98	9.36	4.96	1.35	0.81	0.47	2.64	2.85	0.9

Chinese National Standard GB/T 3299-2011 (2012). The weight of the dry samples is G_1. After boiling, the surface of the sample was wiped off from moisture and weighed (G_2). The water absorption (W) of the sample was calculated as follows:

$$W = \frac{G_2 - G_1}{G_1} \times 100\%. \quad (2)$$

The chemical resistance was measured by using HCl and NaOH as corrosion medium. Two grams of samples was immersed in leaching solutions with 0.01 mol·L^{-1} HCl or 0.01 mol·L^{-1} NaOH at 95 °C for 1 h. At least five samples were measured to take the average value in each experiment. Weight loss was then measured for the chemical durability evaluation.

2.5 Infrared spectroscopy, scanning electron microscopy and Raman spectroscopy characterization

Fourier Transform infrared (FTIR) spectra of the glass-ceramics were obtained with a Nicolet-is10 spectrophotometer in frequency range between 400 and 4000 cm^{-1}. Mixtures of KBr and sample powders were pelleted using a hydraulic press. The contribution of KBr was canceled out by normalizing the spectrum of each sample to the spectrum of KBr. High-resolution images using scanning electron microscope (SEM) were obtained with a Carl Zeiss EVO 18. The glass surfaces were etched with diluted HF (5 vol%) prior to the recording of the SEM images. LabRam-1B Raman spectroscope was used for measurements at room temperature. The 532.04-nm-line He–Ne laser was used as the excitation source. The time of spectrometer integration was 1000 s. All spectra were recorded three times between 300 and 1800 cm^{-1} with a precision of ± 1 cm^{-1} and averaged. The Raman spectrum data were fitted by Gaussian function with an aid of the ''Peak Fit'' program. This fitting procedure yielded ± 0.5% error limit. The content of Q^n (Q represents the tetrahedral unit and n represents the number of bridging oxygen per tetrahedron) was calculated from the area fraction of the fitted Gaussian curves.

3 Results and discussion

3.1 Crystallization kinetics of CMAS glasses

The endothermic and exothermic peaks of the DSC curves are related to nucleation and crystallization, respectively [15]. During the crystallization process, phase separation, nucleation and crystal growth all occur at crystallization peak temperatures (T_p). One crystallization exothermic peak is shown in DSC curves at the heating rate of 10, 15 and 25 K·min^{-1}. The crystallization peak temperatures (T_p) are marked in Fig. 1. It can be seen in Fig. 1 that the crystallization exothermic peak temperature (T_p) increases with the heating rate. DSC curves of the parent glass powders at different heating rates are given in Fig. 1a, b. The onset of the temperature slope change in the thermogram was taken as glass transition temperature (T_g) [16]. The maximum exothermic peak temperature of the GC-3 sample is higher than that of GC-1 sample. In general, the crystallization temperature changes with the composition of the parent glass changes. As the heating rate increases, the rate of crystal phase transformation increases. The crystallization exothermic peaks therefore become sharper at a faster heating rate.

The crystallization dynamics of a glass can be calculated with the modified Kissinger equation [17]. The activation energy was calculated using the linear dependence of the Kissinger Equation as described by Eq. (3).

$$\ln\frac{\alpha}{T_p^2} = -\frac{E_a}{RT_p} + C \quad (3)$$

where α is the DSC heating rate, E_a is the crystallization activation energy, R is the gas constant, and C is the constant. A plot of $\ln(\alpha/T_p^2)$ versus $1000/T_p$ is shown in Fig. 1c. The activation energy can be calculated by a linear fitted plot of $\ln(\alpha/T_p^2)$ versus $1000/T_p$. The value of crystal growth index (n) was calculated with the Augis–Bennett equation.

$$n = \frac{2.5}{\Delta T} \cdot \frac{RT_p^2}{E_a} \quad (4)$$

where ΔT is the full width at half maximum of the exothermic peak intensity. The crystal growth index (n), crystallization activation energy and coefficients of

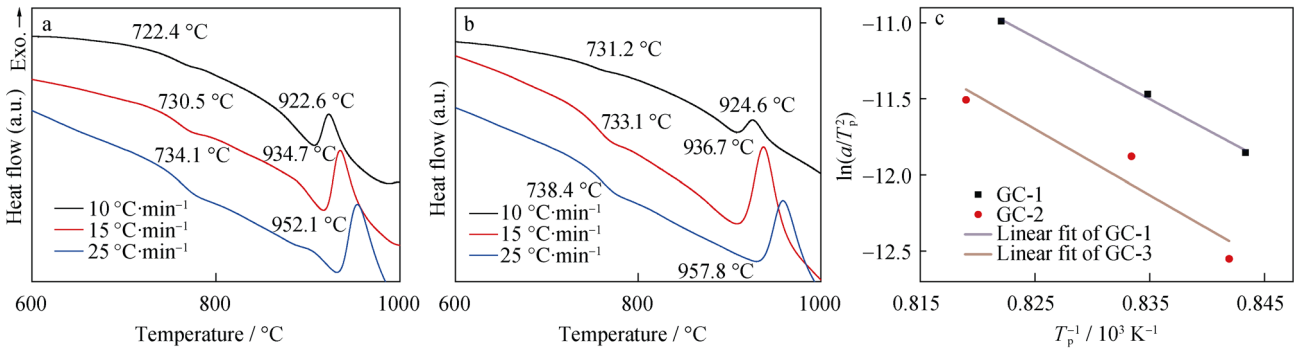

Fig. 1 DSC curves at heating rates of 10, 15 and 25 K·min^{-1} of **a** GC-1 and **b** GC-3; **c** variation of $\ln(\sigma/T_p^2)$ versus $1000/T_p$ for GC-1 and GC-3

determination (R^2) are given in Table 3. The R^2 vales are 0.9981 and 0.9997, respectively, indicating that the activation energy data are reliable.

The calculated activation energy (E_a) is the energy barrier when the glass matrix transforms into the crystallized phase. In previous work [11], it was shown that a higher E_a value resulted in difficulties during nucleation and crystallization. Lower E_a value means that the transition from a glass to crystallize is relatively easier [18]. The comparison of calculated E_a values for GC-1 and GC-3 samples shows that activation energy increases as basicity decreases, and therefore the activation energy of GC-3 sample is higher than that of GC-1 sample. This implies that the high value of basicity improves the crystallization ability of the CMAS glass.

The crystallization behavior of glass-ceramics is related to the Avrami index (n). When $n = 1$, surface crystallization dominates and when $n = 2$, two-dimensional growth is thermodynamically favored. When the Avrami index (n) is greater than 3, three-dimensional crystallization is favored. The n values of each glass-ceramic sample are listed in Table 3. The results indicate that a high value of basicity promotes the three-dimensional crystallization.

3.2 Crystalline phases and microstructure of CMAS glass-ceramics

The composition and microstructure of the main crystal phase are important factors that affect the material properties of the glass-ceramics. In order to study the effect of basicity on the crystal phase composition and microstructure morphology, XRD analysis of the crystallized glass was carried out. Figure 2 shows XRD patterns of the glass-ceramics heat-treated at 922 °C for 1 h. The major phase of all samples is augite (Ca(Mg, Fe, Al)$(SiAl)_2O_6$; PDF No. 24-0203). As the basicity changes, the main crystal phase of glass-ceramics is augite, and a second phase formation is observed. The secondary phase is donathite ($(Ca,Mg)(Cr,Fe)_2O_4$, PDF No. 22-0349). With basicity increasing, the peak positions in XRD patterns of augite are shifted to a lower angle. The shift in peak position may be due to the partial substitution of Mg^{2+} for Fe^{2+} in the augite phase, which causes the crystal lattice parameters to increase.

SEM images of the samples obtained at 922 °C after 60 min of heat treatment at this temperature are shown in Fig. 3. The microstructures of glass-ceramics are compact with low porosity and small crystallite size. The edges and corners appear in grains and in granular form. The morphology of the grains indicates the three-dimensional crystal growth. The overall crystallization of glass-ceramics is consistent with the crystal growth index (n), as seen in Fig. 3. The granular crystallites are dispersed homogeneously in the sample. None of the crystallites show the abnormal growth, indicating a good thermal stability.

Table 3 Crystallization activation energy (E_a), crystal growth index (n) values and coefficients of determination for different T_p (R^2)

Samples	E_a/(kJ·mol^{-1})	n	R^2
GC-1	336.0	4	0.99
GC-3	360.7	4	0.81

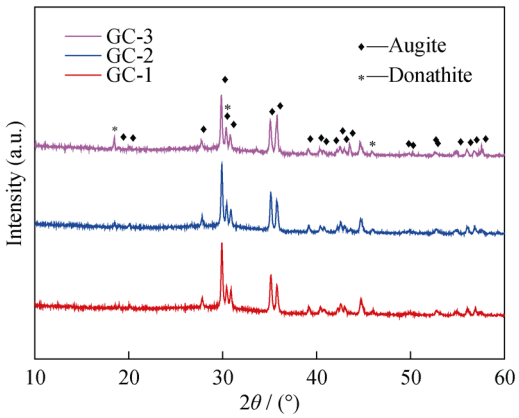

Fig. 2 XRD patterns of GC-1, GC-2 and GC-3 samples

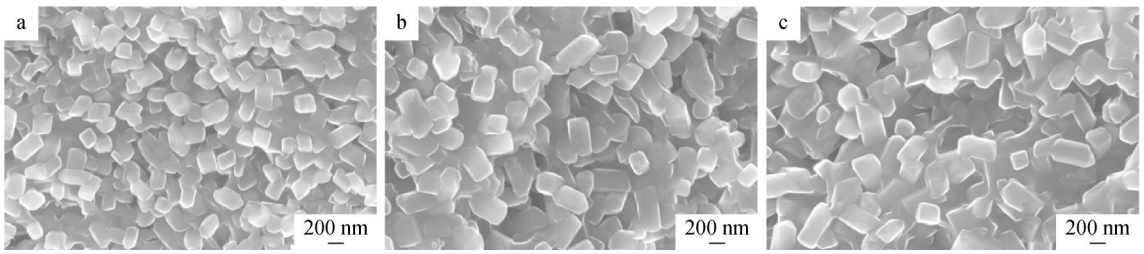

Fig. 3 SEM images of **a** GC-1, **b** GC-2 and **c** GC-3 samples heated at 922 °C for 60 min

Average crystallite sizes of each sample are listed in Table 4. The average crystallite size of GC-1 (281 nm) is smaller than those of GC-2 (351 nm) and GC-3 (359 nm). Usually, the amorphous glass will separate into a residual glass phase and phase-separated regions during heat treatment. The compositions of phase-separated regions are enriched in elements that are similar to the resulting crystal nucleus. A high content of Ca and Mg is shown to result in significant changes to the interfacial tension of the phase or in modification of the glass structure. These changes may give rise to high rates of ionic diffusion. Additionally, phases where the concentration of Ca and Mg cations is concentrated act as heterogeneous nucleation sites. A high tendency to phase separation will reduce the nucleation barrier, and the nucleation activation energy (E_a) will decrease. The reduction in basicity could significantly affect the rates of ionic diffusion [19], which decreases the probability of crystallization. This explains the larger particles of grains measured in GC-3 (Fig. 3). The results show that a high basicity improves the "open degree" of the glass network and increases the rate of the crystallization process.

3.3 Physical and chemical properties of samples

The physical and chemical properties of the three samples are shown in Table 4. The samples were heat-treated at 922 °C for 1 h. The density indicates the competition between the size and mass of the structural units in a glass. The density of glass-ceramics is related to the iconicity and how tightly packed these ions are in the structure. The number of bridging oxygen per unit volume of the glasses (n_b) is closely related to the density [20].

$$n_b = \frac{N_a}{V_m}\sum (n_f X)_i \tag{5}$$

where N_A is the Avogadro's number, V_m is the molar volume, n_f is the coordination number of the glass component, and x_i is the molar fraction of ith oxide. The molar volume (V_m) is calculated with Eq. (6).

$$V_m = \sum \frac{X_i M_i}{\rho} \tag{6}$$

where M_i is the molecular weight of ith component.

As the basicity decreases, the density of the sample increases, which is consistent with other reports in Ref. [21]. While the density increases from 2.47 to 2.90 cm^{-3}, the bridge oxygen content increases from 1.18 to 1.34×10^{21} cm^{-3}. The high value of bridging oxygen per unit volume indicates a high network connectivity. The positive correlation between sample density and bridging oxygen content indicates that the glass network becomes more connective and rigid with basicity decreasing. The network connectivity of the glasses is discussed later.

The results in Table 4 show that the glass-ceramics samples are substantially non-absorbent and are resistant to both acids and alkalis. In Table 4, it is noticeable that average crystal size of GC-1 is smaller than those of GC-2 and GC-3 samples. SEM images (Fig. 3) show that GC-1 sample has the largest grain packing density. The edges and corners appear in grains and in granular form. The denser the grain boundaries are in the material, the more difficult it is for microcracks to spread. Thus, the hardness of GC-1 sample is greater than those of GC-2 and GC-3

Table 4 Physical and chemical properties of GC-1, GC-2, and GC-3 annealed at T_p for 1 h

Samples	ρ/(g·cm^{-3})	$n_b/10^{21}$ cm^{-3}	Hardness/GPa	Bending strength/MPa	Water absorption/wt%	Chemical resistances/wt%	
						HCl	NaOH
GC-1	2.47	1.18	7.33 ± 0.05	120.4 ± 0.7	0.01	0.75	0.02
GC-2	2.61	1.23	7.28 ± 0.05	117.7 ± 0.8	0.01	0.74	0.03
GC-3	2.90	1.34	7.17 ± 0.03	114.3 ± 0.5	0.01	0.22	0.01

samples. This result coincides with the result reported by Peng et al. [22] that fine-grained glass-ceramics possess harder mechanical properties. In the case of the studied compositions, the properties of glass-ceramics prepared from industrial raw materials are similar to those prepared by Gao (ρ is 2.517 g·cm^{-3}, and bending strength is 77.04 MPa) [8]. The results of this study demonstrate that steel slag and fly ash can be used for preparing glass-ceramics. The measured material properties of the glass-ceramics suggest that these would be for industrial and construction applications.

3.4 Infrared absorption spectra of samples

The structures building units of the prepared glass-ceramics were studied using FTIR spectra (Fig. 4). The FTIR spectra show that the glass-ceramics contain different molar ratios of silicon and oxygen. The band located at approximately 490 cm^{-1} is assigned to a Si–O–Si bending vibration mode [22]. The band near 450–600 cm^{-1} is attributed to the bending and rocking motions of the silicate network. The absorption band at 484 cm^{-1} is present from bending vibrations of Al–O–Al or Al–O–Si bonds. The band attributed to the scission of the Si–O–Si chain occurs at 750 cm^{-1} [23]. The bands in the range of 850–1200 cm^{-1} are assigned to the symmetric stretch vibrations of the [SiO_4] tetrahedron with different bridging oxygens (BOs) [24, 25]. As seen from the difference spectrum in Fig. 4, the bridge oxygen content in GC-3 sample is significantly higher than that of GC-1 sample. As seen in FTIR spectra, the half-widths of the bands are slightly different. It can be concluded that the different cations in the glass-forming oxides influence the final glass structural bonding. A large half-width of absorption peaks makes it difficult to distinguish the respective types of vibrational modes.

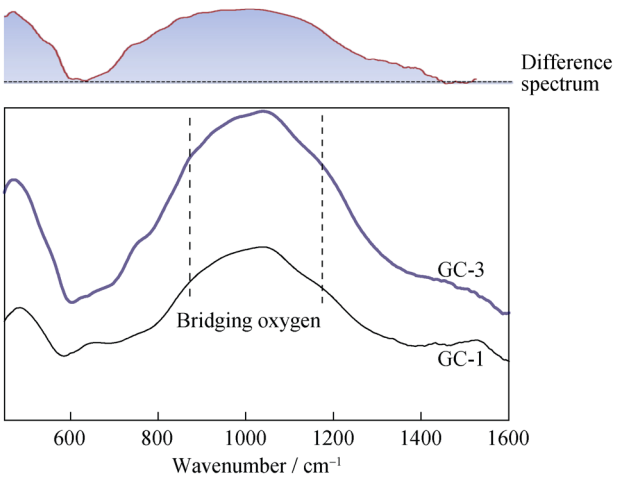

Fig. 4 FTIR absorption spectra of GC-1 and GC-3 samples

3.5 Raman spectrum analysis

To gain insights into the structural changes that occur with changes in basicity, a deconvoluted Raman was measured. The value of Q^n was calculated from the area fraction of the fitted Gaussian curves. The band between 900 and 920 cm^{-1} is assigned to Si–O$^-$ bond with one bridging oxygen per SiO_4 tetrahedron stretching vibration (Q^1 group) (Q^n being SiO_4 tetrahedron with bridging oxygen). The band at 950–980 is characteristic of asymmetric stretch vibrations of Si–O bonds with two bridging oxygen (Q^2). The band at 1150–1100 is characteristic of asymmetric stretch vibrations of Si–O bonds with three bridging oxygen (Q^3). The shoulder at 850–880 cm^{-1} is attributed to the Q^0 unit. The assignment of bands around 1120 and 1190 cm^{-1} is the presence of fully polymerized units (Q^4). Raman spectra between 800 and 1300 cm^{-1} fit with four Gaussian peaks: 860 cm^{-1} (Q^0), 905 cm^{-1} (Q^1), 965 cm^{-1} (Q^2), 1060 cm^{-1} (Q^3) and 1150 cm^{-1} (Q^4), respectively [26, 27]. In GC-1 and GC-3 samples, the scattering of Q^4 could not be resolved due to the very low intensity in the parent glass. This result is also confirmed by theoretical molecular dynamics (MD) calculations [28]. A high content of BO in a glass results in a rigid, highly connective and more polymerized glass network. The bands at 950–980 cm^{-1} are characteristic of asymmetric stretch vibrations of Si–O bonds with two bridging oxygen (Q^2). The bands at 1150–1100 are characteristic of asymmetric stretch vibrations of three bridging oxygens (Q^3). The contribution of Q^2 is to depolymerize the glass network. Table 5 shows the different ratios of $Q^3/(Q^2 + Q^1)$, which can signify glass network polymerization. Thus, at a lower basicity, glass structure becomes rigid due to the dominant formation of Q^3. According to these results, polymerization of the glass network increases with the decrease in basicity.

The comparison of Fig. 5a and Fig. 5b shows that a lower content of modifier oxides enhances the vibration of Q^3, while the vibration of Q^1 and Q^0 is weakened. This indicates that more silicon and aluminum enter the glass network. With an increasing amount of glass-forming oxides in the glass structure, an improved structural ordering of the ions is achieved. This result is consistent with the number n_b, which is listed in Table 4 and may be

Table 5 Peak area ratio obtained from a Gaussian deconvolution of Raman spectra

Samples	$Q^3/(Q^2 + Q^1)$	Best fitted Gaussian peak area ratio			
		Q^0	Q^1	Q^2	Q^3
GC-1	0.19	0.087	0.246	0.520	0.146
GC-3	0.24	0.071	0.195	0.554	0.181

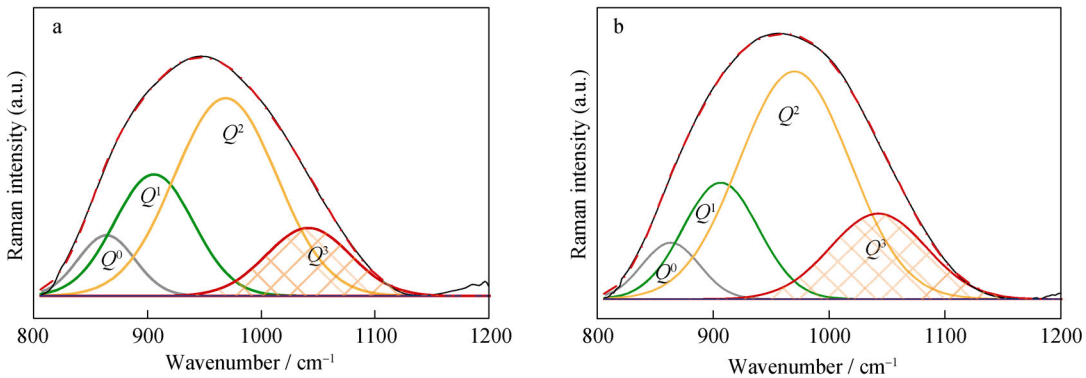

Fig. 5 Typical deconvolution of Raman spectra of **a** GC-1 and **b** GC-3 samples

due to several reasons. Firstly, CaO and MgO contents decrease as basicity decreases, the number of bridge oxygen in the glass network increases, resulting in polymerization of the glass network. Secondly, the addition of Al_2O_3 produces more AlO_4 tetrahedrons and forms a unified network as silicon tetrahedron SiO_4 further increases the glass network connectivity. Finally, as the SiO_2 content in the glass phase increases, the number of bridge oxygen increases and the polymerization of the glass network increases. The high degree of polymerization of glass network suppresses ionic diffusion, phase separation [29, 30] and growth of crystal nuclei [1], which are promoted by the increase in E_a. This result is supported by calculated values of the activation energy, and GC-3 sample has a higher activation energy than GC-1 sample.

4 Conclusion

Glass-ceramics were successfully produced from industrial stainless steel slag and fly ash. The $(CaO + MgO)/(SiO_2 + Al_2O_3)$ ratios of the solid waste raw materials during the preparation of the glass -ceramics were studied. The activation energy increases from 336.0 to 360.7 $kJ \cdot mol^{-1}$ with the decrease in the $(CaO + MgO)/(SiO_2 + Al_2O_3)$ ratio. All results given in this work, along with the preceding discussion, indicate that the mechanism of crystallization is affected by basicity (the $(CaO + MgO)/(SiO_2 + Al_2O_3)$ ratio), which could be evidenced by the reduction of modifier oxides and the increase in glass-forming oxides. As the content of modifier oxides (Ca and Mg ions) decreases, the number of non-bridging oxygen in the glass networks decreases. When the content of glass-forming oxides (SiO_2 and Al_2O_3) in the glass networks increases, the number of bridging oxygen increases. This phenomenon increases the degree of polymerization of the glass network, as revealed by a decrease in relative distribution of Q^0 and Q^1 units and an increase in Q^3 structural groups. When Q^3 increases the polymerization, the rigidity of the glass structure increases. Consequently, the ions undergoing a rearrangement process (crystallization) requires more thermal energy in a high degree of polymerization of the glass network, which would result in the process being less cost-effective. The result indicates that the production of the glass-ceramics from industrial steel slag and fly ash is cost efficient with an optimized $(CaO + MgO)/(SiO_2 + Al_2O_3)$ ratio.

Acknowledgements This study was financially supported by the National Natural Science Foundation of China (Nos. U1360202, 51472030, 51672024 and 51502014), the Fundamental Research Funds for the Central Universities (No. FRF-TP-16-027A3) and the Innovation Project of Yunnan Province New Material Preparation and Processing Key Laboratory (No. 2016cx05).

References

[1] Yang J, Liu B, Zhang S, Volinsky AA. Glass–ceramics one-step crystallization accomplished by building Ca^{2+} and Mg^{2+} fast diffusion layer around diopside crystal. J Alloys Compd. 2016; 688:709.
[2] Păcurariu C, Lazău I. Non-isothermal crystallization kinetics of some glass–ceramics with pyroxene structure. J Non-Cryst Solids. 2012;358(23):3332.
[3] Karpukhina N, Hill RG, Law RV. Crystallisation in oxide glasses-a tutorial review. Chem Soc Rev. 2014;43(7):2174.
[4] Fan W, Liu B, Xun L, Yang J, Guo B, Zhang S. Production of glass–ceramics using municipal solid waste incineration fly ash. Rare Met. https://doi.org/10.1007/s12598-017-0976-8.
[5] Pelino M. Recycling of zinc-hydrometallurgy wastes in glass and glass ceramic materials. Waste Manag. 2000;20(7):561.
[6] Dai W, Li Y, Cang D, Liu Z, Fan Y. BOF slag glass–ceramics prepared in different atmospheres from parents glasses with various reduction degree. ISIJ Int. 2014;54(12):2672.
[7] Zheng W, Cao H, Zhong J, Qian S, Peng Z, Shen C. CaO–MgO–Al_2O_3–SiO_2 glass–ceramics from lithium porcelain clay tailings for new building materials. J Non-Cryst Solids. 2015; 409:27.
[8] Gao R, Wang H, Zhu Q, Yang Q, Sun X, Li B, Xu S, Zhang X. The forming region and mechanical properties of SiO_2–Al_2O_3–MgO glasses. J Non-Cryst Solids. 2017;470:132.
[9] Partyka J, Sitarz M, Lesniak M, Gasek K, Jelen P. The effect of SiO_2/Al_2O_3 ratio on the structure and microstructure of the

glazes from SiO_2–Al_2O_3–CaO–MgO–Na_2O–K_2O system. Spectrochim Acta A. 2015;134:621.
[10] Xiao H, Cheng Y, Yu L, Liu H. A study on the preparation of CMAS glass–ceramics by in situ crystallization. Mater Sci Eng A. 2006;431(1–2):191.
[11] Fan W, Liu B, Yang J, Zhang S. The influence of Na_2O on the fast diffusion layer around diopside crystals. RSC Adv. 2017; 7(16):9417.
[12] Khater GA. Influence of Cr_2O_3, LiF, CaF_2 and TiO_2 nucleants on the crystallization behavior and microstructure of glass–ceramics based on blast-furnace slag. Ceram Int. 2011;37(7):2193.
[13] Lu Z, Lu J, Li X, Shao G. Effect of MgO addition on sinterability, crystallization kinetics, and flexural strength of glass–ceramics from waste materials. Ceram Int. 2016;42(2): 3452.
[14] Rezvani M, Eftekhari-Yekta B, Solati-Hashjin M, Marghussian VK. Effect of Cr_2O_3, Fe_2O_3 and TiO_2 nucleants on the crystallization behaviour of SiO_2–Al_2O_3–CaO–MgO(R_2O) glass–ceramics. Ceram Int. 2005;31(1):75.
[15] Yang J, Zhang S, Pan D, Liu B, Wu C, Volinsky AA. Treatment method of hazardous pickling sludge by reusing as glass–ceramics nucleation agent. Rare Met. 2016;35(3):269.
[16] Azín NJ, Camerucci MA, Cavalieri AL. Crystallisation of non-stoichiometric cordierite glasses. Ceram Int. 2005;31(1): 189.
[17] Dong J, Yu Y, Xue Z. Non-isothermal kinetics of synthesizing vanadium nitride by one-step method. Rare Met. 2015;34(10): 738.
[18] Zhang SG, Yang J, Liu B, Pan DA, Wu CL, Volinsky AA. One-step crystallization kinetic parameters of the glass–ceramics prepared from stainless steel slag and pickling sludge. J Iron Steel Res. 2016;23(3):220.
[19] Casasola R, Pérez JM, Romero M, Pinckney L. Crystal growth of F-phlogopite from Glasses of the SiO_2–Al_2O_3–MgO–K_2O–F system. J Am Ceram Soc. 2016;99(2):484.
[20] Zamyatin OA, Plekhovich AD, Zamyatina EV, Sibirkin AA. Glass-forming region and physical properties of the glasses in the TeO_2–MoO_3–Bi_2O_3 system. J Non-Cryst Solids. 2016;452: 130.
[21] Doweidar H. Density of CaO–Al_2O_3–SiO_2 glasses with (CaO/Al_2O_3) $\geq$ 1; the hidden factors. J Non-Cryst Solids. 2017;471: 344.
[22] Peng F, Liang KM, Hu AM. Nano-crystal glass-ceramics obtained from high alumina coal fly ash. Fuel. 2005;84(4):341.
[23] Dantas NO, Ayta WE, Silva AC, Cano NF, Silva SW, Morais PC. Effect of Fe_2O_3 concentration on the structure of the SiO_2–Na_2O–Al_2O_3–B_2O_3 glass system. Spectrochim Acta A. 2011;81(1):140.
[24] Goel A, Shaaban ER, Tulyaganov DU, Ferreira JMF. Study of crystallization kinetics in glasses along the diopside-Ca-Tschermak join. J Am Ceram Soc. 2008;91(8):2690.
[25] Kiani ZM, Rezvani M, Asadi TR. Crystallization, sinterability and microwave dielectric properties of CaO–SiO_2–Na_2O–MgO glass ceramics containing Fe_2O_3 and ZnO. Electron Mater Lett. 2014;10(1):131.
[26] Manara D, Grandjean A, Neuville DR. Advances in understanding the structure of borosilicate glasses: a Raman spectroscopy study. Am Miner. 2009;94(5–6):777.
[27] Chen L, Wang TS, Zhang GF, Yang KJ, Peng HB, Zhang LM. XPS and Raman studies of electron irradiated sodium silicate glass. Chin Phys B. 2013;22(12):126101.
[28] Wu YQ, Jiang GC, You JL, Hou HY, Chen H, Xu KD. Theoretical study of the local structure and Raman spectra of CaO-SiO_2 binary melts. J Chem Phys. 2004;121(16):7883.
[29] Jindal R, Jayaganthan R, Singh IV, Conradt R. Synthesis and characterization of clinopyroxene based glasses and glass–ceramics along diopside ($CaMgSi_2O_6$)-jadeite ($NaAlSi_2O_6$) join. Ceram Int. 2011;37(3):741.
[30] Sheng JW, Huang BX, Zhang J, Zhang H, Sheng JY, Yu S, Zhang MJ. Production of glass from coal fly ash. Fuel. 2003; 82(2):181.